Spinning worlds

Schwarz, H.

4 Spin measurement of the substellar companion GSC 6214-210 b with CRIRES

In collaboration with:
Matteo Brogi, Ignas Snellen, Jayne Birkby, Remco de Kok
In preparation

The rotational velocities of exoplanets and brown dwarf companions are fundamental observables which affects their climate, atmospheric dynamics, and magnetic field, and may hold important clues to the formation process and the orbital history of these objects. We have measured the projected rotational velocity of the young, directly imaged, substellar companion GSC 06214-00210 b, which has a well-determined mass straddling the planet – brown dwarf boundary. Rotation period data are available in the literature for very low-mass stars and brown dwarfs, both in open clusters and in the field, but substellar companions present a unique challenge due to their close proximity to a bright host star. We combine spectral and spatial filtering to separate the signal of the companion from that of the host star by observing the target in the near-infrared with a high-dispersion slit spectrograph using adaptive optics. The companion spectrum is optimally extracted and cross-correlated with a template spectrum, and the rotational broadening is measured from the shape of the cross-correlation signal. We detect carbon monoxide with a signal-to-noise of 5.3 in the atmosphere of GSC 06214-00210 b and measure the projected rotational velocity to be $v \sin(i) = 21.5 \pm 3.5\,\mathrm{km\,s^{-1}}$. That is similar to the $v \sin(i)$ measured for the exoplanet β Pictoris b, but significantly faster than that for GQ Lupi b.

4.1 Introduction

Climate and atmospheric dynamics can be strongly affected by the spin rate of a planet. A faster rotation period for the Earth would have a profound effect on ocean and wind circulation patterns and the redistribution of solar energy around the globe, leading to a greater temperature difference from equator to pole (Showman et al., 2013). The spin rate plays an equally important role in the case of gas giants.

Showman et al. (2015) discuss the effects of rotation on warm and hot Jupiters, and Showman and Kaspi (2013) focus on brown dwarfs and directly imaged planets, the former of which are generally fast rotators causing the large-scale flows to be rotationally dominated. Also the occurrence and strength of a magnetic field are closely linked to planet rotation (Parker, 1955; López-Morales et al., 2011).

It is clear that planets acquire their angular momenta during the early formation process, when they accrete the bulk of their masses. Unlike low-mass stars, that can lose a large fraction of their spin through magnetic breaking, planets are more likely to retain their angular momenta except through gravitational interactions. The details of how angular momentum is accreted are less clear. Generally, two formation processes are considered for giant planets: i) core accretion, where gas accretes onto planetary embryos of several Earth masses (Pollack et al., 1996; Laughlin et al., 2004; Hubickyj et al., 2005), and ii) disk fragmentation, where gas rapidly collapses on itself due to a disk gravitational instability in the outer protoplanetary disk (Boss, 1997, 2000). If core accretion and disk fragmentation result in differences in spin angular momenta, it is possible this will show up in studies of the spin of substellar companions as a function of mass and of orbital distance, which could be a proxy for different formation scenarios.

The solar system planets have a wide range of spin velocities which show an increasing trend with planetary mass (Hughes, 2003). The Earth and Mars rotate relatively slowly with spin rates of 24 to 25 hours and equatorial rotation velocities of 465 $\mathrm{m\,s^{-1}}$ and 241 $\mathrm{m\,s^{-1}}$, respectively. Neptune and Uranus rotate in 16 to 17 hours with velocities around 2.6 $\mathrm{km\,s^{-1}}$, while Jupiter and Saturn rotate significantly faster in 10 to 11 hours with 12.6 $\mathrm{km\,s^{-1}}$ and 9.9 $\mathrm{km\,s^{-1}}$, respectively. Mercury and Venus have equatorial rotation velocities that fall below the spin $-$ mass relation observed in the remaining planets, but this can be explained by the tidal interactions with the Sun that have significantly slowed them down. Also, the Earth has been slowed somewhat owing to tidal energy dissipation by the Moon. Surprisingly, Uranus does follow the trend while its obliquity is $\sim 98^{\circ}$, pointing to a catastrophic event.

Two observational methods are available to measure the spin of an extrasolar body. The first makes use of temporal photometric variations caused by local variations in the surface brightness that can be monitored during rotation. In the case of substellar companions, this requires high-contrast direct imaging techniques to separate the starlight from that of the faint companion. It has been applied to the exoplanet 2M1207 b exhibiting flux modulations indicating a rotation period of 10.7 hours (Zhou et al., 2016). The second method, as used in this paper, combines high-dispersion spectroscopy with high-contrast imaging to separate the light from the companion from that of the star, and subsequently

the projected rotational velocity ($v \sin(i)$) is measured through the width of absorption lines in the thermal spectrum of the companion. Although this is not a direct measurement of the rotation period, since the viewing geometry is generally unknown, the method does not depend on the presence of surface brightness variations, it is more straightforward to interpret, and it can be performed in relatively short observing time - if the appropriate instrumentation is available. In this way, our group observed the exoplanet β Pictoris b with the Very Large Telescope (VLT) and the instrument the Cryogenic High-Resolution Infrared Echelle Spectrograph (CRIRES; Kaeufl et al., 2004), measuring it to have a $v \sin(i)$ of 25 km s^{-1} (Snellen et al., 2014). Just before CRIRES was taken off the telescope for a major upgrade, we were awarded time to conduct a small survey to measure the $v \sin(i)$ of three additional substellar companions to further investigate the spin properties of wide-orbit, young companions. Observations of GQ Lupi b are discussed in Schwarz et al. (2016, $v \sin(i) = 5.3$ km s^{-1}), and those of HIP 78530 b will be presented in a forthcoming paper. Here we describe the observations and results for GSC 06214-00210 b (hereafter GSC 6214 b), which has an age and a mass in between those of β Pictoris b and GQ Lupi b.

In Section 2 we characterise the GSC 6214 system, and in Section 3 we give the details of the observations. The data analysis is explained in Sections 4 and 5: Section 4 is the basic data reduction and the extraction of the companion spectrum, and Section 5 is the cross-correlation analysis which we employ to measure the rotational broadening of the molecular lines in the thermal spectrum of the companion. The results are presented and discussed in Section 6.

4.2 The GSC 06214-00210 system

GSC 6214 A is a pre-main-sequence, solar-type star in Upper Scorpius, which is a subgroup of the nearest OB association. Members of Upper Scorpius have a small age dispersion (Preibisch and Mamajek, 2008), with a typical age initially estimated by low-mass evolutionary models to be 5 Myr (Preibisch et al., 2002), and more recently revised to 11 Myr (Pecaut et al., 2012), based on isochrone fitting. The 16 M_J companion GSC 6214 b was discovered by Ireland et al. (2011) with adaptive optics imaging. It is seen to orbit at a projected distance of 320 au, and there is unambiguous evidence for a circumplanetary accretion disk (Bowler et al., 2011; Lachapelle et al., 2015; Zhou et al., 2014). The dust mass of this disk is constrained to less than 0.15 $M_\oplus$ by observations from the Atacama Large Millimeter/submillimeter Array (ALMA; Bowler et al., 2015), and GSC 6214 b is therefore not expected to gain significant mass. More information about the system is given in Table 5.1.

Table 4.1: GSC 06214-00210 system properties

Property	GSC 6214 A[i]	GSC 6214 b[ii]
Teff [K]	4200 ± 150	2300 ± 200
Spectral type	K7 $\pm$ 0.5	M9γ $\pm$ 0.5
Mass	0.9 ± 0.1 M$_\odot$	16 ± 1.5 M$_J$
Surf. grav. log(g)	4.0	
Distance [pc][iii]	145 ± 20	
Age [Myr][v]	11 ± 2	
Ang. sep. ["][ii]	2.17 ± 0.02	
ΔK [mag][ii]	5.74 ± 0.01	

[i] Bowler et al. (2011)
[ii] Lachapelle et al. (2015)
[iii] de Zeeuw et al. (1999)
[v] Pecaut et al. (2012)

4.3 Observations

We observed the GSC 6214 system on 29 May 2014 as part of the ESO programme 293.C-5012(A). The observations were carried out with the infrared high-dispersion spectrograph CRIRES (Kaeufl et al., 2004) at the Very Large Telescope on Cerro Paranal in Chile. We obtained a standard set of calibration frames and eight science exposures of 300 seconds each. We used the smallest slit width of 0.2″ to maximise the spectral resolution, which is close to 90 000. The slit was aligned with the position angle of the companion ($PA = 175.2°$, Zhou et al., 2014), thus observing the host star and the companion simultaneously. With a K-band contrast ratio between the companion and the host star of 5.06×10^{-3} (Lachapelle et al., 2015), and an angular separation of 2.2″, these are high contrast observations. We made use of the Multi Application Curvature Adaptive Optics system (MACAO, Arsenault et al., 2003) to both suppress the star light and maximise the throughput. The observations were carried out under clear sky conditions, at airmasses below 1.02, hence very close to zenith, and with seeing of 1″. The telescope was nodded sequentially in an ABBA pattern along the slit direction between positions A and B, 10″ apart, to allow accurate background subtraction. Additionally, a small random offset was introduced for each exposure to improve flatfielding and hot pixel corrections.

The CRIRES instrument has four Aladdin III InSB detectors each spanning 1024 x 512 pixels with physical separations between the detectors corresponding

to approximately 280 pixels. We observed at 2.3 μm targeting the ro-vibrational (2, 0) R branch of carbon monoxide, with the standard wavelength settings for order 24. Additional absorption from water vapour is also likely to be present at these wavelengths.

4.4 Data analysis

The basic data reduction was performed with recipes from the CRIRES pipeline version 2.3.2 and processed with the EsoRex tool version 3.10.2. The raw science frames were dark-subtracted, flatfielded, and corrected for known bad pixels and non-linearity effects. Furthermore, EsoRex was used to perform the background subtraction by combining the science frames in AB nodding pairs, and to optimally extract (Horne, 1986) a one-dimensional spectrum of the star GSC 6214 A from each of the four AB-combined frames. The remainder of the data analysis was carried out with custom-built Python scripts, unless specifically stated otherwise.

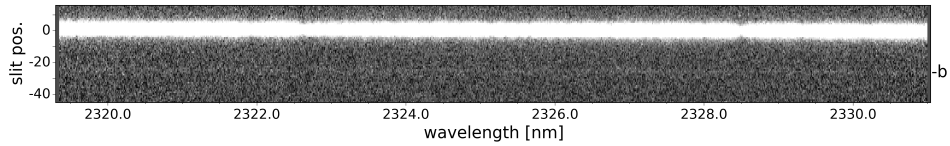

Figure 4.1: An example of a two-dimensional spectrum from detector 3, after the basic data reduction steps and cropped to the relevant slit positions. The bright band is the spectral trail of the star. Twenty-six pixels below, the faint trail of the companion can be seen (marked with *b*).

We cropped the combined frames in the spatial direction (i.e. along the slit) close to the positions of the stellar spectrum and the companion spectrum. The automatic bad pixel correction in the CRIRES pipeline is insufficient and therefore we visually identified remaining detector defects and cosmic rays using the programme *SAOImage DS9*. The bad pixels were corrected with cubic spline interpolation based on the four nearest neighbours within the same row. A few detector defects were severe enough that it was necessary to mask out entire columns from the subsequent data analysis. This was the case for 32 columns in the second detector, 65 columns in the fourth detector, as well as the four columns closest to the left and right edge of all detectors. Fig. 5.2 is one of the AB-combined frames from the third detector. The faint spectral trail of the companion is visible 26 pixels below the stellar spectral trail.

We opted to discard the first detector from the analysis, based on the combined

effects of a well-known non-linearity issue[1] causing a high noise level, and very little expected signal due to few CO lines in that part of the wavelength range. The fourth detector suffers from the same non-linear effects, but this was adequately corrected by the non-linearity procedure of the pipeline. Unfortunately, we have also had to discard the first and second AB-combined frames from all detectors, leaving only half of the data set. The first frame suffers from an unknown systematic issue across the entire wavelength range, which has caused severe non-linearity from row to row. The second frame was exposed as the target passed zenith, and the violent slewing of the telescope caused the companion not to be within the slit throughout the exposure.

4.4.1 Extraction of the companion spectrum

From the carefully cleaned frames, we performed an optimal extraction of the companion spectra with the IRAF procedure *apall*. The fitted trace of the stellar spectral trail was applied as a reference and manually offset to the position of the companion, which could easily be identified by summing together 100-500 wavelength bins. We found this to be well-matched by the pixel distance determined from the plate scale and the literature value for the angular separation. The background of scattered stellar light was ignored at this stage and was instead removed manually as described in section 4.4.3. We extracted a companion spectrum from each detector and AB-combined frame.

4.4.2 Wavelength calibration and the systemic velocity

We determined the wavelength solution in an iterative process of refining trial wavelength solutions based on cross-correlating the average observed stellar spectrum and a template spectrum which contained both stellar molecular lines and telluric lines. The Doppler shift of the stellar lines in the model was allowed to vary at every step of the iteration so that we could simultaneously measure the unknown radial velocity (RV) of the star.

The wavelength calibration was performed separately for each detector. The change in the Doppler shift of the stellar lines due to the rotation and the orbital motion of the Earth is negligible over the course of the 40 minutes of the observations, and therefore it is sufficient to calibrate the average observed spectrum. We constructed template spectra for a range of Doppler shifts by multiplying a Doppler shifted PHOENIX model and a synthetic transmission spectrum from ESO SkyCalc. The details of the models are given in table 4.2. Both the telluric

[1] http://www.eso.org/sci/facilities/paranal/instruments/crires/doc/VLT-MAN-ESO-14500-3486_v93.pdf

model and the stellar model was convolved to a spectral resolution of 90 000, which is a typical value for the actual resolving power of CRIRES. This provided a visually good fit to the telluric lines, and although the fit of the stellar lines was imperfect, we found that it was sufficient for the wavelength calibration. Both the Doppler shifted Phoenix model and the telluric model were interpolated to a trial wavelength solution before they were multiplied and cross-correlated with the observed spectrum. The initial trial solution was taken from a previous CRIRES data set, published in Schwarz et al. (2016).

Table 4.2: The template spectra in the wavelength calibration routine were constructed from the following individual models

GSC 6214-210 A model: PHOENIX
Teff 4200 K log(g) 4.0 solar metallicity http://phoenix.astro.physik.uni-goettingen.de Husser et al. (2013)
Sky transmission model: ESO SkyCalc
Airmass 1.0 PWV seasonal https://www.eso.org/observing/etc/skycalc Noll et al. (2012); Jones et al. (2013)

The final wavelength solution was determined in an iterative process of refining the trial solutions to maximise the cross-correlation coefficient while allowing the Doppler shift of the stellar lines to vary. This method is an adaptation of the iterative wavelength calibration in Brogi et al. (2016). Following Brogi et al. (2016), the trial wavelength solutions are quadratic fits to all possible combinations of five evenly spaced wavelength guesses for the first, the middle and the last pixel of the detector. This corresponds to a total of 125 trial solutions. For each iteration, we selected the provisional best wavelength solution based on the highest cross-correlation coefficient and let this solution form the central triplet of pixel-wavelength pairs in the following iteration, where the wavelength step size between guesses was refined. We found that for all detectors the cross-correlation coefficient improved with each iteration until a step size corresponding to 10% of a pixel (Fig. ??), and also at this step size the best radial velocity of the star converged to a single value (Fig. ??). Accordingly, we estimated that the accuracy of the final wavelength solution was 10% of a pixel, and applying the heliocentric correction of $-0.06\,\mathrm{km\,s^{-1}}$, the systemic velocity of GSC 6214 A was measured to be $-5.3 \pm 0.1\,\mathrm{km\,s^{-1}}$.

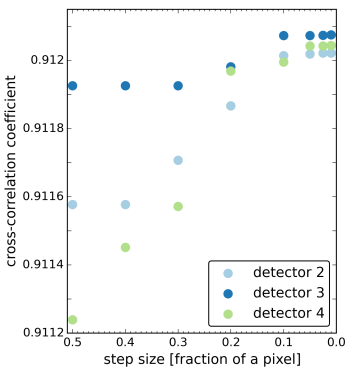

(A) The accuracy of the wavelength solutions continued to improve with iterations until a step size corresponding to 10% of a pixel.

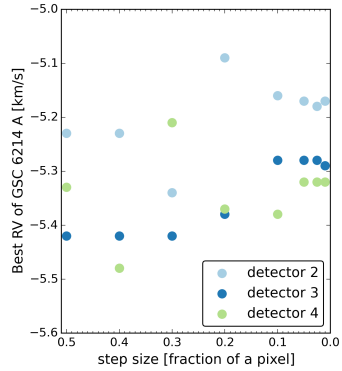

(B) The measured RV-values for GSC 6214 A, corrected for the rotation and the orbit of the Earth.

Figure 4.2: The wavelength solution was determined in an iterative process of cross-correlating the observed stellar spectrum and a template spectrum. For each iteration the best wavelength solution (i.e. the one with the highest cross-correlation coefficient) from a set of 125 trial solutions was selected and the step size defining the grid of solutions was refined. The radial velocity of the star was measured at every iteration of the wavelength calibration by cross-correlating with template spectra where the stellar lines had a range of Doppler shifts relative to the stationary telluric lines.

4.4.3 Removing the stellar and telluric background

At the position of the companion, the flux is dominated by the companion itself with the stellar flux suppressed to a level of 20% of that of the companion. The observed stellar spectrum including telluric lines was scaled to this contrast ratio and subtracted.

For removing the telluric lines in the companion spectrum, we made use of the same telluric model which was applied in the template used for the wavelength calibration (Table 4.2). The telluric model was carefully fitted to the average observed stellar spectrum to adjust the line profiles to the instrumental profile. First, the observed stellar spectrum including telluric lines was flattened, i.e. the continuum gradient was removed by fitting the continuum with a polynomial and dividing with the fit. The telluric model and the stellar model (also as used for the wavelength calibration, Table 4.2) were both downsampled to the wavelength solution and the stellar model was Doppler shifted to the measured radial velocity of the star. Then, the stellar model was adjusted to the observed stellar spectrum by con-

volving with a broadening kernel determined with singular value decomposition (SVD; Rucinski, 1999), and the observed stellar spectrum was divided with this stellar fit, thus providing the observed telluric spectrum. Subsequently, the telluric model was adjusted to the observed telluric spectrum, again by convolving with an SVD broadening kernel. This resulted in a telluric model with the correct line profiles broadened by the instrument profile, which was then scaled to the mean level of the companion spectrum and subtracted. The influence of contamination from the Earth's atmosphere on the companion spectrum is very small for this data set. The final companion spectrum is shown in Fig. 4.4, and is the weighted average of the two frames with the weights determined from the cross-correlation analysis (Sec. 4.5.2).

4.5 Measuring the $v \sin(i)$

The thermal spectrum of the companion has absorption lines from molecules present in the companion atmosphere and when observed at the high spectral resolution of CRIRES, the molecular bands are resolved into individual lines. The rotation of the object causes a broadening of the spectral lines due to the redshifts of the receding half of the surface and the blueshifts of the approaching half. In other words, the broadening reveals the component of the spin velocity projected along the line of sight, and thus provides a minimum value for the objects rotational velocity. However, the extracted companion spectrum of GSC 6214 b has a low signal-to-noise (S/N), and it is not possible to measure the broadening of the individual lines directly. Instead, we combine the signal from all the spectral lines within the wavelength range by cross-correlating with a template spectrum. The cross-correlation function will have a peak if the relative positions of the spectral lines of the model match those of the observed spectrum, and by using models with a single trace gas the presence of specific gas molecules in the atmosphere can be unambiguously detected. Most importantly, the cross-correlation profile is highly sensitive to the shape of the spectral lines in the observed spectrum, and therefore the projected rotational velocity can be measured from the cross-correlation function.

4.5.1 The template spectra

At the high temperatures of a young object like GSC 6214 b, the most abundant trace gas molecules in the K-band are expected to be CO and H_2O (Barman et al., 2015; Moses et al., 2016). We modelled the thermal spectrum of GSC 6214 b with the single-trace gas and double-trace gas template spectra, which were gen-

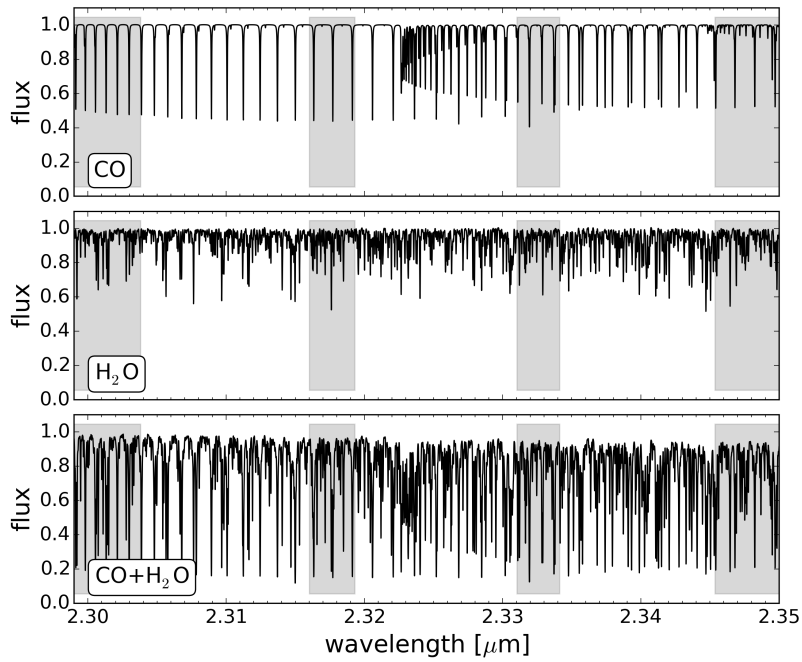

Figure 4.3: The template spectra which were used in the cross-correlation analysis. The top two panels show the models with either CO or H_2O as a single-trace gas, and the lower panel shows the model containing both CO and H_2O. The three models have temperatures that decrease with a constant lapse rate from 2150 K at 1 bar to 1100 K at 0.03 bar, and the T/p profiles are isothermal outside of this pressure range. The volume mixing ratios for CO and H_2O are 10^{-4} both in the single-trace gas and double-trace gas models. The gaps between the three detectors are shaded in grey.

erated for GQ Lupi b by Schwarz et al. (2016). These models employ the line lists from HITEMP 2010 (Rothman et al., 2010), and assume collision-induced absorption by hydrogen (Borysow et al., 2001; Borysow, 2002). The temperature-pressure profiles (T/p profiles) were parameterised the following way: They are isothermal at pressures higher than p_0 = 1 bar with a temperature of T_0 = [1650 K, 1900 K, 2150 K], and the temperature decreases with a constant lapse rate (i.e. the rate of temperature change with log pressure) until it reaches T_1 = [750 K, 1100 K, 1450 K, 1800 K] at pressure p_1 = [$10^{-1.5}$ bar, $10^{-2.5}$ bar, $10^{-3.5}$ bar, $10^{-4.5}$ bar]. The models are isothermal again at higher altitudes or equivalently lower pressures. Both CO and H_2O were tested with four different volume mixing ratios, VMR = [$10^{-5.5}$, $10^{-5.0}$, $10^{-4.5}$, $10^{-4.0}$]. The model spectra were convolved to the spectral resolution of CRIRES, which we have measured to be $\sim$ 90 000, prior to cross-correlation. Fig. 4.3 illustrates the three example models from the T/p grid.

4.5.2 Cross-correlation analysis

We performed the cross-correlation individually per frame and detector, and the analysis was carried out for every template spectrum in the T/p grid described in Sec. 4.5.1. The model was Doppler-shifted over the range -250 to $250\,\mathrm{km\,s^{-1}}$, and the individual companion spectra were cross-correlated with the model for every RV step of $1.5\,\mathrm{km\,s^{-1}}$. We will refer to the cross-correlation function (CCF) from the companion spectrum and a template spectrum as the measured CCF. The designations for the different types of cross-correlation functions that are used in this paper are summarised in Table 4.3. The model has not been subjected to rotational broadening, so the absorption lines are relatively narrow with a width dominated by the instrumental profile, which we have applied to all the models. Assuming the molecule of the model is present in the companion atmosphere, the cross-correlation of the narrow-lined model with an observed spectrum with rotationally broadened lines will produce a cross-correlation signal centred on the radial velocity of the companion, and the shape of the signal will be closely related, though not identical, to the average line profile of the observed spectrum.

Table 4.3: Nomenclature for the cross-correlation functions

Designation	Spectrum 1 $\star$ Spectrum 2
measured CCF	companion spec. $\star$ model $v \sin(i) = 0$
broad meas. CCF	companion spec. $\star$ model $v \sin(i) \neq 0$
injected CCF	injected spec. $\star$ model $v \sin(i) = 0$
(narrow) auto-CF	model $v \sin(i) = 0$ $\star$ model $v \sin(i) = 0$
broad auto-CF	model $v \sin(i) \neq 0$ $\star$ model $v \sin(i) \neq 0$
model CCF	model $v \sin(i) = 0$ $\star$ model $v \sin(i) \neq 0$

CCF = cross-correlation function; auto-CF = auto-correlation function; spec. = spectrum; meas. = measured

In order to determine appropriate weighting of the frames and detectors, we resampled the model at the observed wavelengths and injected it into the measured companion spectrum:

$$\text{inj\_spec.} = \text{comp\_spec.} + \text{model} * mean(\text{comp\_spec.}) \tag{4.1}$$

The injected spectrum was cross-correlated with the model spectrum, and the difference between this injected CCF and the measured CCF represents the expected cross-correlation signal from a given model, and it is sensitive to both the strength and the number of spectral lines for a given detector. Although this step is performed for each frame, the expected signal is unique to each model and detector,

and independent of the data quality. On the other hand, the measured CCF does contain information about the data quality, because it is sensitive to the S/N of the companion spectrum as obtained from the individual frames of a detector. Both effects are combined in a form of S/N weights:

$$w = \left(\frac{max(\text{injected CCF} - \text{measured CCF})}{std(\text{measured CCF})} \right)^2 \tag{4.2}$$

The weights were normalised and they constitute a set of detector weights and frame weights which were used both separately and together, depending on the context. In particular the weights were applied to the cross-correlation functions of the individual frames and detectors to construct the weighted averages of any cross-correlation functions considered in the remainder of this paper. The frame weights were also applied when combining the companion spectra from the individual frames to the final weighted average spectrum of GSC 6214 b, which is displayed in Fig. 4.4.

We fit the signal of the measured CCF with model CCFs, in order to measure the projected rotational velocity and the radial velocity of the companion. The model CCFs were constructed by cross-correlating the non-broadened model spectrum with rotationally broadened and shifted versions of the model itself. We tested projected rotational velocities in the range 0 to 60 km s^{-1} and Doppler shifts in the range -20 to 10 km s^{-1}. For both parameters the step size was 0.5 km s^{-1}. Thereafter, each of these model CCFs was offset (y-direction) and scaled with a least-squares fit to best match the measured companion CCF. Finally, we determined the best-fit model CCF, and by extension the best-fit $v \sin(i)$ and RV, through $\mathcal{X}^2$ minimisation, along with confidence intervals from rescaling the errors so $\bar{\mathcal{X}}^2 = 1$. The measured radial velocity was corrected to the heliocentric radial velocity, i.e. it was compensated for the relative radial velocity of the observer at the time of observation, caused by the spin rotation of Earth and the orbital motion around the Sun.

4.6 Results & Discussion

The final spectrum of the substellar companion GSC 6214 b is shown if Fig. 4.4, with the rotationally broadened CO model overplotted in red. The S/N of the spectrum in detectors 2, 3, and 4 are $\sim$0.9, 1.1, and 1.5, respectively. This striking difference is mirrored in the spectrum of the host star, and in fact the continuum flux of the stellar spectral trail was seen to increase gradually from the shorter to the longer wavelengths. The cause of the wavelength dependence is unknown but must have an instrumental origin. It has no influence on the results: The detector

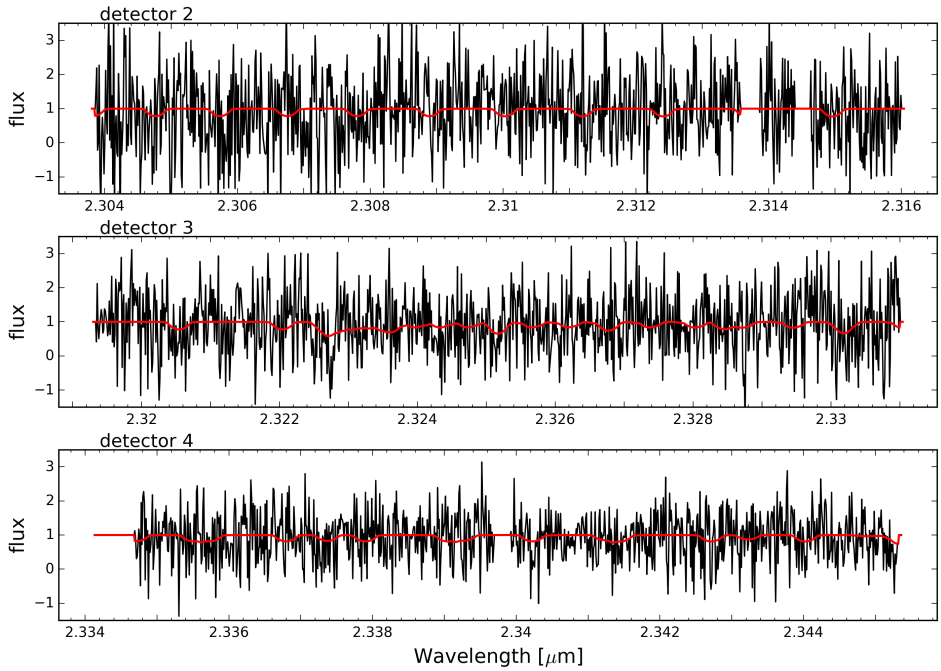

Figure 4.4: The thermal spectrum of GSC 6214 b (black). The individual frames were combined as a weighted average, where the weights were determined as part of the cross-correlation analysis, as described in Sec. 4.5.2. The red line is the CO model from the top panel of Fig. 4.3, convolved to the CRIRES resolution, rotationally broadened to match the measured $v \sin(i)$ of 21.5 km s^{-1}, and Doppler shifted to match the expected radial velocity. Although the companion spectrum is dominated by noise, some of the more prominent CO lines are discernible in detectors 3 and 4.

weights in the cross-correlation analysis are sensitive to the S/N of the companion spectrum, as well as to the number and strength of lines for a given detector (Sec. 4.5.2). In general, due to the low S/N, the individual CO lines of the thermal spectrum are hidden within the noise, but hints of the most prominent absorption lines can be identified in detectors 3 and 4.

Subsequently, the presence of specific individual molecules is best revealed from cross-correlating with single-trace-gas model spectra. Fig. 4.3 shows the CO, H_2O, and CO+H_2O model spectra from Schwarz et al. (2016), which we have used in the cross-correlation analysis. The displayed models are representative of the tested model grid, and we find that at the low S/N of these observations, the results are insensitive to a wide range of T/p profiles. The example models share the same T/p profile and have a temperature that decreases from 2150 K at 1 bar

to 1100 K at 0.03 bar and is isothermal outside this pressure range.

We detect CO in the atmosphere of GSC 6214 b, but we cannot confirm the presence of H_2O from these observations. The measured cross-correlation function using the CO single-trace gas model is shown by the solid black line in Fig. 5.6. The lower panel is a magnification of the relevant region. The cross-correlation function shows a distinct and broadened CO signal centred around a radial velocity close to the systemic velocity. Cross-correlation using the double-trace gas model give rise to a similar, yet slightly weaker signal, and the H_2O model shows no hint of a signal.

The profile of the measured CO cross-correlation signal is broadened, and the narrow auto-correlation function of the CO model is a poor fit. The auto-CF is shown in Fig. 5.6 as the black dotted line. This is a clear indication that the absorption lines of the companion spectrum are rotationally broadened. We have fitted the measured CCF with model CCFs of varying $v \sin(i)$-values and Doppler shifts, as described in Sec. 4.5. The best-fit model CCF is determined from χ^2 minimisation, and it is shown as the red solid line in Fig. 5.6, and the shading indicates the 2σ confidence. We find that the projected rotational velocity of GSC 6214 b is $21.5 \pm 3.5\,\mathrm{km\,s^{-1}}$, whereas a Doppler shift relative to the systemic velocity ($5.3\,\mathrm{km\,s^{-1}}$, Sec. 4.4.2) was not unambiguously detected.

The significance of the CO detection cannot be deduced from the measured cross-correlation function of the companion spectrum and the CO model, because the narrow lines of the model are not a good match to the rotationally broadened lines present in the observed companion spectrum. Instead, we cross-correlated the companion spectrum with the model rotationally broadened by the best-fit $v \sin(i) = 21.5\,\mathrm{km\,s^{-1}}$, and then adopted the S/N of this broad measured CCF:

$$\frac{S}{N} = \frac{max(\text{broad meas. CCF})}{std(\text{broad meas. CCF} - \text{broad auto-CF})} \tag{4.3}$$

The signal is the peak value of the broad measured CCF, and the noise is the standard deviation of the broad measured CCF minus the auto-correlation function of the rotationally broadened model. From this, we find that CO is detected in the atmosphere of GSC 6214 b with a S/N of 5.3.

The radii of directly-imaged planets cannot be measured directly as in the case of transiting planets, and have to be inferred from evolutionary models and/or connecting their effective temperature to their luminosity. In the case of GSC 6214 b, we estimate the current radius to be approximately $1.7 \pm 0.2\,\mathrm{R_J}$ based on evolutionary models (Burrows et al., 2001), and thus the companion is expected to spin up to $37 \pm 7\,\mathrm{km\,s^{-1}}$ when it ultimately contracts to the size of Jupiter. This implies that the rotation period of the sub-stellar companion is currently ∼9-10 hours, and is expected to decrease to ∼3-4 hours.

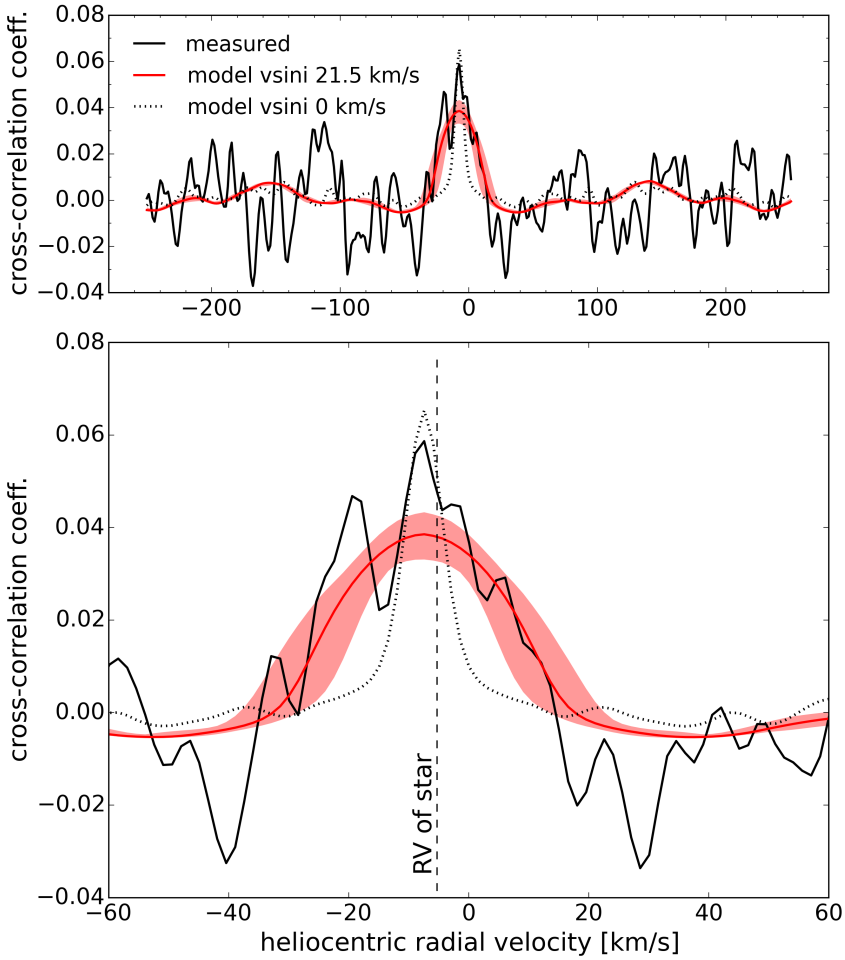

Figure 4.5: The cross-correlation function (CCF) from the CO model with narrow absorption lines and the observed companion spectrum (solid black line). The peak, centred at an RV close to that of the host star, shows that GSC 6214 b has CO in the atmosphere. The black dotted line is the auto-correlation function of the CO model, scaled and offset to best match the measured CCF. It can be seen that the measured CO signal is broader than the auto-correlation signal. We find that the measured CCF is well fit by a model CCF from the CO model and a rotationally broadened version of itself with a vsini of 21.5 $\mathrm{km\,s^{-1}}$. This best fit model CCF is shown as the red solid line, and the shading indicates the 2σ confidence. As for the auto-correlation function, the broader model CCF has been scaled and offset with a least-square fit to the measured CCF. The lower panel is an enlarged version of the central radial velocities of the upper panel.

We measure the radial velocity, corrected for the heliocentric motion, of GSC 6214 b to be $-7.6 \pm 2.0\,\mathrm{km\,s^{-1}}$. This is consistent within the 2σ errorbars with the systemic velocity of the host star ($-5.3\,\mathrm{km\,s^{-1}}$), which was measured as part of the wavelength calibration routine in Sec. 4.4.2. The expected circular orbital velocity of GSC 6214 b is $1.6\,\mathrm{km\,s^{-1}}$ at the observed orbital distance of 320 au. Therefore, the RV measurement is well within the expected range. Unfortunately, the S/N of these observations are not sufficient to further constrain the orbit, like in the case of GQ Lupi b (Schwarz et al., 2016) and β Pictoris b (Snellen et al., 2014).

Only three other substellar companions have measurements of their spin rotation: β Pictoris b and 2M1207 b which are likely of planetary mass, and GQ Lupi b which has a highly uncertain masses, straddling the planet – brown dwarf boundary. β Pictoris b and GQ Lupi b both have $v\sin(i)$ measurements (Snellen et al., 2014; Schwarz et al., 2016) and are a part of the CRIRES survey that this work is based upon, and 2M1207 b has a measurement of the rotation period (Zhou et al., 2016) from which the equatorial rotation velocity can be inferred. Their rotational velocities (either $v\sin(i)$ or v_{eq}) are plotted as a function of mass in Fig. 4.6. The rotational velocity of GSC 6214 b falls in between those of β Pictoris b and 2M1207 b, and GQ Lupi b appears as an outlier with a rotational velocity 3 to 5 times slower than the others.

We can speculate that the initial angular momentum content of a substellar companion will depend on its specific formation scenario (e.g. core accretion versus disk fragmentation) and its total accreted mass. However, the observable - the spin velocity or rotation period - will also depend on its current state of evolution. E.g. the objects can still be accreting matter and angular momentum. Also, they will significantly spin-up to faster rotational velocities during their contraction and cooling phase. The sample of substellar companions with measured spin rates currently available is too small to disentangle these different processes. However, we see that the youngest object in the sample, GQ Lupi b (<5 Myr), indeed exhibits the slowest rotation pointing to an evolutionary effect. GSC 6214 b is of intermediate age (11 Myr) within the sample, and rotates significantly faster than GQ Lupi b, with a velocity that is comparable to the β Pictoris b and 2M1207 b measurements. However, GSC 6214 b is also more massive than those two, and in the light of the mass-spin relation as seen in our solar system, it may be expected that more massive planets rotate faster. Both GQ Lupi b and GSC 6214 b are actively accreting material (e.g. Zhou et al., 2014), but in the case of GSC 6214 b the dust mass of the accretion disk has been constrained by ALMA observations to less than 0.15 $M_\oplus$ (Bowler et al., 2015), meaning that GSC 6214 b is not expected to gain significant mass or angular momentum from accretion. Of course,

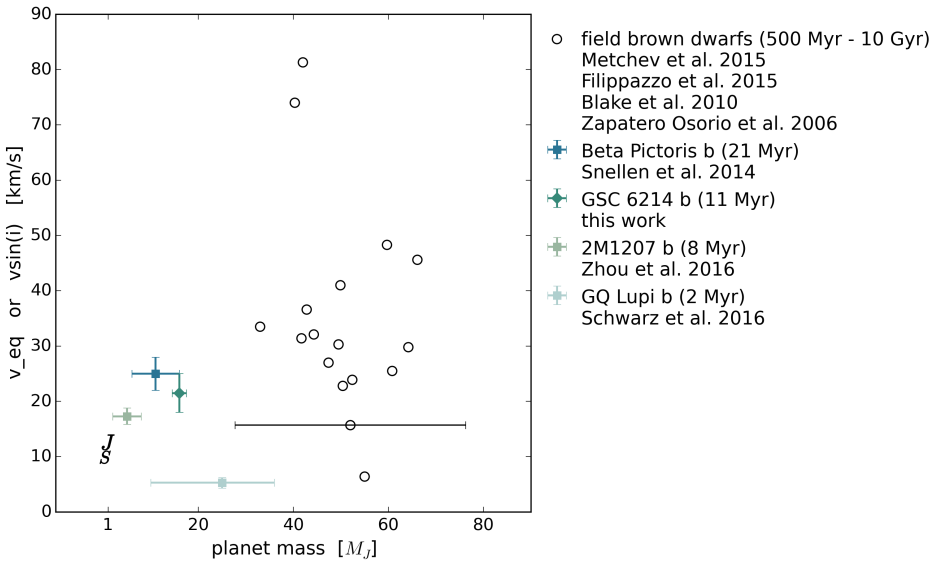

Figure 4.6: Spin as a function of mass for extrasolar substellar companions, together with Jupiter and Saturn, and a sample of field brown dwarfs. The solar system planets and 2M1207 b have equatorial rotation velocities and β Pictoris b, GQ Lupi b and GSC 6214 b have projected rotational velocities. For comparison, field brown dwarfs with estimated masses and either a rotational period measurement or $v \sin(i)$ measurement are shown as empty circles, with the typical uncertainty in mass indicated for a single object.

on an object to object basis, the obliquity can also play a major role, meaning that comparative analyses can only be conducted in a strict statistical way with a larger sample.

4.7 Conclusions

We successfully observed the substellar companion GSC 06214-00210b with the high-dispersion CRIRES spectrograph on ESO's Very Large Telescope at 2.3 μm targeting the carbon monoxide band. CO is detected at a S/N of 5.3 but H_2O is not seen. We measure a projected rotational velocity of $21.5 \pm 3.5\,\mathrm{km\,s^{-1}}$ from fitting the shape of the CO cross-correlation signal with model cross-correlation functions with varying rotational broadening. The radial velocity of the companion is consistent with that of the star, as expected for the wide orbital separation of 320 au.

References

Arsenault, R., J. Alonso, H. Bonnet, J. Brynnel, B. Delabre, R. Donaldson, C. Dupuy, E. Fedrigo, J. Farinato, N. N. Hubin, L. Ivanescu, M. E. Kasper, J. Paufique, S. Rossi, S. Tordo, S. Stroebele, J.-L. Lizon, P. Gigan, F. Delplancke, A. Silber, M. Quattri, and R. Reiss
2003. MACAO-VLTI: An Adaptive Optics system for the ESO VLT interferometer. In *Adaptive Optical System Technologies II*, P. L. Wizinowich and D. Bonaccini, eds., volume 4839 of *Society of Photo-Optical Instrumentation Engineers (SPIE) Conference Series*, Pp. 174–185.

Barman, T. S., Q. M. Konopacky, B. Macintosh, and C. Marois
2015. Simultaneous Detection of Water, Methane, and Carbon Monoxide in the Atmosphere of Exoplanet HR8799b. *ApJ*, 804:61.

Blake, C. H., D. Charbonneau, and R. J. White
2010. The NIRSPEC Ultracool Dwarf Radial Velocity Survey. *ApJ*, 723:684–706.

Borysow, A.
2002. Collision-induced Absorption Coefficients of H_2 Pairs at Temperatures from 60 K to 1000 K. *A&A*, 390:779.

Borysow, A., U. G. Jørgensen, and Y. Fu
2001. High-temperature (1000-7000k) Collision-induced Absorption of H_2 Pairs Computed from the First Principles, with Application to Cool and Dense Stellar Atmospheres. *J. Quant. Spec. Radiat. Transf.*, 68(3):235.

Boss, A. P.
1997. Giant planet formation by gravitational instability. *Science*, 276:1836–1839.

Boss, A. P.
2000. Possible Rapid Gas Giant Planet Formation in the Solar Nebula and Other Protoplanetary Disks. *ApJ*, 536:L101–L104.

Bowler, B. P., S. M. Andrews, A. L. Kraus, M. J. Ireland, G. Herczeg, L. Ricci, J. Carpenter, and M. E. Brown
2015. An ALMA Constraint on the GSC 6214-210 B Circum-substellar Accretion Disk Mass. *ApJ*, 805:L17.

Bowler, B. P., M. C. Liu, A. L. Kraus, and A. W. Mann
2014. Spectroscopic Confirmation of Young Planetary-mass Companions on Wide Orbits. *ApJ*, 784:65.

Bowler, B. P., M. C. Liu, A. L. Kraus, A. W. Mann, and M. J. Ireland
2011. A Disk around the Planetary-mass Companion GSC 06214-00210 b: Clues about the Formation of Gas Giants on Wide Orbits. *ApJ*, 743:148.

Brogi, M., R. J. de Kok, S. Albrecht, I. A. G. Snellen, J. L. Birkby, and H. Schwarz
2016. Rotation and Winds of Exoplanet HD 189733 b Measured with High-dispersion Transmission Spectroscopy. *ApJ*, 817:106.

Burrows, A., W. B. Hubbard, J. I. Lunine, and J. Liebert
2001. The theory of brown dwarfs and extrasolar giant planets. *Reviews of Modern Physics*, 73:719–765.

de Zeeuw, P. T., R. Hoogerwerf, J. H. J. de Bruijne, A. G. A. Brown, and A. Blaauw
1999. A HIPPARCOS Census of the Nearby OB Associations. *AJ*, 117:354–399.

Filippazzo, J. C., E. L. Rice, J. Faherty, K. L. Cruz, M. M. Van Gordon, and D. L. Looper
2015. Fundamental Parameters and Spectral Energy Distributions of Young and Field Age Objects with Masses Spanning the Stellar to Planetary Regime. *ApJ*, 810:158.

Horne, K.
1986. An optimal extraction algorithm for CCD spectroscopy. *PASP*, 98:609–617.

Hubickyj, O., P. Bodenheimer, and J. J. Lissauer
2005. Accretion of the gaseous envelope of Jupiter around a 5 10 Earth-mass core. *Icarus*, 179:415–431.

Hughes, D. W.
2003. Planetary spin. *Planet. Space Sci.*, 51:517–523.

Husser, T.-O., S. Wende-von Berg, S. Dreizler, D. Homeier, A. Reiners, T. Barman, and P. H. Hauschildt
2013. A new extensive library of PHOENIX stellar atmospheres and synthetic spectra. *A&A*, 553:A6.

Ireland, M. J., A. Kraus, F. Martinache, N. Law, and L. A. Hillenbrand
2011. Two Wide Planetary-mass Companions to Solar-type Stars in Upper Scorpius. *ApJ*, 726:113.

Jones, A., S. Noll, W. Kausch, C. Szyszka, and S. Kimeswenger
2013. An advanced scattered moonlight model for Cerro Paranal. *A&A*, 560:A91.

Kaeufl, H.-U., P. Ballester, P. Biereichel, B. Delabre, R. Donaldson, R. Dorn, E. Fedrigo, G. Finger, G. Fischer, F. Franza, D. Gojak, G. Huster, Y. Jung, J.-L. Lizon, L. Mehrgan, M. Meyer, A. Moorwood, J.-F. Pirard, J. Paufique, E. Pozna, R. Siebenmorgen, A. Silber, J. Stegmeier, and S. Wegerer
2004. CRIRES: a high-resolution infrared spectrograph for ESO's VLT. In *Ground-based Instrumentation for Astronomy*, A. F. M. Moorwood and M. Iye, eds., volume 5492 of *Society of Photo-Optical Instrumentation Engineers (SPIE) Conference Series*, Pp. 1218–1227.

Lachapelle, F.-R., D. Lafrenière, J. Gagné, R. Jayawardhana, M. Janson, C. Helling, and S. Witte
2015. Characterization of Low-mass, Wide-separation Substellar Companions to Stars in Upper Scorpius: Near-infrared Photometry and Spectroscopy. *ApJ*, 802:61.

Laughlin, G., P. Bodenheimer, and F. C. Adams
2004. The Core Accretion Model Predicts Few Jovian-Mass Planets Orbiting Red Dwarfs. *ApJ*, 612:L73–L76.

López-Morales, M., N. Gómez-Pérez, and T. Ruedas
2011. Magnetic Fields in Earth-like Exoplanets and Implications for Habitability around M-dwarfs. *Origins of Life and Evolution of the Biosphere*, 41:533–537.

Metchev, S. A., A. Heinze, D. Apai, D. Flateau, J. Radigan, A. Burgasser, M. S. Marley, É. Artigau, P. Plavchan, and B. Goldman
2015. Weather on Other Worlds. II. Survey Results: Spots are Ubiquitous on L and T Dwarfs. *ApJ*, 799:154.

Moses, J. I., M. S. Marley, K. Zahnle, M. R. Line, J. J. Fortney, T. S. Barman, C. Visscher, N. K. Lewis, and M. J. Wolff
2016. On the Composition of Young, Directly Imaged Giant Planets. *ApJ*, 829:66.

Noll, S., W. Kausch, M. Barden, A. M. Jones, C. Szyszka, S. Kimeswenger, and J. Vinther
2012. An atmospheric radiation model for Cerro Paranal. I. The optical spectral range. *A&A*, 543:A92.

Parker, E. N.
1955. Hydromagnetic Dynamo Models. *ApJ*, 122:293.

Pecaut, M. J., E. E. Mamajek, and E. J. Bubar
2012. A Revised Age for Upper Scorpius and the Star Formation History among the F-type Members of the Scorpius-Centaurus OB Association. *ApJ*, 746:154.

Pollack, J. B., O. Hubickyj, P. Bodenheimer, J. J. Lissauer, M. Podolak, and Y. Greenzweig
1996. Formation of the Giant Planets by Concurrent Accretion of Solids and Gas. *Icarus*, 124:62–85.

Preibisch, T., A. G. A. Brown, T. Bridges, E. Guenther, and H. Zinnecker
2002. Exploring the Full Stellar Population of the Upper Scorpius OB Association. *AJ*, 124:404–416.

Preibisch, T. and E. Mamajek
2008. *The Nearest OB Association: Scorpius-Centaurus (Sco OB2)*, P. 235.

Rothman, L. S., I. E. Gordon, R. J. Barber, H. Dothe, R. R. Gamache, A. Goldman, V. I. Perevalov, S. A. Tashkun, and J. Tennyson
2010. HITEMP, the High-Temperature Molecular Spectroscopic Database. *J. Quant. Spec. Radiat. Transf.*, 111(15):2139.

Rucinski, S.
1999. Determination of Broadening Functions Using the Singular-Value Decomposition (SVD) Technique. In *IAU Colloq. 170: Precise Stellar Radial Velocities*, J. B. Hearnshaw and C. D. Scarfe, eds., volume 185 of *Astronomical Society of the Pacific Conference Series*, P. 82.

Schwarz, H., C. Ginski, R. J. de Kok, I. A. G. Snellen, M. Brogi, and J. L. Birkby
2016. The slow spin of the young substellar companion GQ Lupi b and its orbital configuration. *A&A*, 593:A74.

Showman, A. P. and Y. Kaspi
2013. Atmospheric Dynamics of Brown Dwarfs and Directly Imaged Giant Planets. *ApJ*, 776:85.

Showman, A. P., N. K. Lewis, and J. J. Fortney
2015. 3D Atmospheric Circulation of Warm and Hot Jupiters. *ApJ*, 801:95.

Showman, A. P., R. D. Wordsworth, T. M. Merlis, and Y. Kaspi
2013. *Atmospheric Circulation of Terrestrial Exoplanets*, Pp. 277–326.

Snellen, I. A. G., B. R. Brandl, R. J. de Kok, M. Brogi, J. Birkby, and H. Schwarz
2014. Fast spin of the young extrasolar planet β Pictoris b. *Nature*, 509:63–65.

Zapatero Osorio, M. R., E. L. Martín, H. Bouy, R. Tata, R. Deshpande, and R. J. Wainscoat
2006. Spectroscopic Rotational Velocities of Brown Dwarfs. *ApJ*, 647:1405–1412.

Zhou, Y., D. Apai, G. H. Schneider, M. S. Marley, and A. P. Showman
2016. Discovery of Rotational Modulations in the Planetary-mass Companion 2M1207b: Intermediate Rotation Period and Heterogeneous Clouds in a Low Gravity Atmosphere. *ApJ*, 818:176.

Zhou, Y., G. J. Herczeg, A. L. Kraus, S. Metchev, and K. L. Cruz
2014. Accretion onto Planetary Mass Companions of Low-mass Young Stars. *ApJ*, 783:L17.